RESEARCH ARTICLE

Correspondence to:
J. Skákala,
jos@pml.ac.uk

Using multifractals to evaluate oceanographic model skill

Jozef Skákala[1], Pierre W. Cazenave[1], Timothy J. Smyth[1], and Ricardo Torres[1]

[1]Plymouth Marine Laboratory, Plymouth, UK

Abstract We are in an era of unprecedented data volumes generated from observations and model simulations. This is particularly true from satellite Earth Observations (EO) and global scale oceanographic models. This presents us with an opportunity to evaluate large-scale oceanographic model outputs using EO data. Previous work on model skill evaluation has led to a plethora of metrics. The paper defines two new model skill evaluation metrics. The metrics are based on the theory of universal multifractals and their purpose is to measure the structural similarity between the model predictions and the EO data. The two metrics have the following advantages over the standard techniques: (a) they are scale-free and (b) they carry important part of information about how model represents different oceanographic drivers. Those two metrics are then used in the paper to evaluate the performance of the FVCOM model in the shelf seas around the south-west coast of the UK.

1. Introduction

Numerical models are broadly used in oceanography for various different purposes: to improve our insight into phenomena, to supply surrogate data, to predict future conditions, and for the purpose of decision making [*Stow et al.*, 2009]. Satellite measurements provide us with large volumes of data for fields such as sea surface temperature, or ocean surface chlorophyll-a concentrations. These data can be used to test the quality of the model predictions.

Various techniques exist to compare the Earth Observation (EO) and the model data sets and to subsequently evaluate the model performance. The data sets can be compared using statistical parameters such as correlation coefficient, average error, root-mean-square error, reliability index, the cost function, various binary types of metrics, etc. [*Allen et al.*, 2007a,2007b,2008; *Allen and Somerfeld*, 2009; *Doney et al.*, 2008; *Jolliff et al.*, 2009; *Saux Picart et al.*, 2012; *Shutler et al.*, 2011; *Stow et al.*, 2009; *Taylor*, 2001]. These tools form the standard set of model skill evaluation metrics [*Stow et al.*, 2009; *Taylor*, 2001].

The standard model skill evaluation metrics are of major importance and offer a powerful way of looking at model performance. However, these methods have their weaknesses: they are typically scale-dependent and do not necessarily reflect on structural similarities between two data sets. Scale dependency biases the metrics by phenomena specific to the scale of analysis. The second point, the incapability of metrics to reflect on structural similarities can be shown on a simple example: imagine an extremely heterogeneous distribution and create another distribution by spatially shifting the first distribution. If the original distribution was sufficiently heterogeneous, a slight "phase shift" between the two distributions can lead to a very small mutual correlation and large mean square errors. If one of those distributions was a model output and the other is the EO data, the standard metrics would completely disqualify the model performance despite the fact that the two data sets are nearly identical (only slightly out of phase).

There is currently only limited number of tools used to assess the structural similarity of the model and the EO data sets, examples of such tools being the self-organizing maps [*Kohonen*, 2000; *Radic and Clarke*, 2011] and wavelet analysis [*Saux Picart et al.*, 2012]. The wavelet analysis has also an additional advantage of comparing the data sets on a range of scales. As different dynamical drivers scale differently, a scale-free metric could provide a unique tool to assess how well the different drivers are represented by the model. To our knowledge neither wavelets, nor any other of the currently used metrics offers a clear analysis of the model performance in terms of specific dynamical drivers. The purpose of this paper is to develop and test two new model skill evaluation metrics that achieve three goals at the same time: the metrics are scale-free,

they compare the data structural properties, and they link those structural properties to the dynamical drivers.

It has been known now for several decades that many phenomena in physics, biology, or even in finance have the property of scale-invariance [*Harte*, 2001; *Lovejoy and Schertzer*, 2013; *Mandelbrot*, 1982, 1997]. One suggested answer to the question of why scale-invariance occurs frequently in nature is a phenomenon called self-organized criticality [*Bak et al.*, 1987]. Heuristically, the emergence of scale-invariance can be understood from the phenomenological equations if, within a certain range of scales, one can neglect all terms that contain dimensional constants. The phenomenological equations without those terms are by definition scale-free. Although the deterministic solutions of those (in general nonlinear) equations describe complicated structures which are subject to chaotic dynamics, the statistics across those structures preserves the symmetry of scale-invariance. Furthermore, unless there is some external discretization condition (such as the presence of physical boundaries), the scale-invariance is *continuous*. Thus, it can be generally expected that such scale-free phenomenological models produce (chaotic looking) data described by statistical models that are scale-invariant at a continuous range of scales.

Continuous scale-invariance is a mathematically significantly constraining property and only a few specific classes of continuous scale-invariant models are known [*Seuront et al.*, 2005]. From the known models the most successful are the stable attractive cascades termed *universal multifractals* [*Schertzer and Lovejoy*, 1987, 1988, 1997, 2011]. The statistical model of universal multifractals has been widely used to model the Earth atmosphere [*Lovejoy et al.*, 2001a; *Lovejoy and Schertzer*, 2010; *Schertzer and Lovejoy*, 1988; *Schmitt et al.*, 1993], the Earth topography [*Gagnon et al.*, 2006; *Lavalee et al.*, 1993], climate [*Lovejoy and Schertzer*, 2013; *Lovejoy*, 2014], and also the oceanic fields [*Lovejoy et al.*, 2001b; *de Montera et al.*, 2011; *Seuront et al.*, 1996a,1996b; *Seuront and Lagadeuc*, 1997; *Seuront et al.*, 1999; *Seuront and Schmitt*, 2005a,2005b; *Skakala and Smyth*, 2015]. Universal multifractals lead to models exhaustively described by the values of three parameters. Therefore, despite a complex system's dynamics being complicated, its statistics can have remarkable simplicity and, using system symmetries, one can reduce it to information about three parameters.

The central idea of this work is a development of metrics comparing data sets via the universal multifractal scaling parameters. This brings us back to the three goals stated earlier in the paper: the universal multifractal type of metrics are automatically scale-free and they tell us how well models reproduce the structural scaling patterns of the EO data. Since the universal multifractal parameters frequently relate to specific dynamical drivers [*Lovejoy et al.*, 2001b; *Skakala and Smyth*, 2015], these metrics also carry relatively straightforward information about which drivers are, or are not, well represented by the oceanographic model.

2. Methods

2.1. Theoretical Background

Universal multifractals have direct links to the theory of turbulence [*Schertzer and Lovejoy*, 1987, 2011; *Schmitt et al.*, 1993]. In the turbulent regime the viscosity term in the Navier-Stokes equation (term containing the dimensional viscosity parameter) can be neglected when compared to the nonlinear inertia and the Navier-Stokes equation becomes scale-free. There is a characteristic energy input scale which breaks scale-invariance on large scales, but at intermediate scales, scales in between the energy input scale and the viscosity scale (usually being of the order of millimeter), the turbulent eddies governed by the scale-free Navier-Stokes equation statistically dissipate in a scale-invariant way [*Gurvitch and Yaglom*, 1967; *Kolmogorov*, 1941; *Novikov and Stewart*, 1964; *Obukhov*, 1949; *Richardson*, 1922; *Yaglom*, 1966]. The eddies lead to the following length correlations in the fluid longitudinal velocity (*v*) components [*Kolmogorov*, 1941]:

$$\Delta v_\ell \equiv \langle v(x+\ell) - v(x) \rangle \simeq \langle \epsilon_\lambda^{1/3} \rangle \ell^{1/3}. \tag{1}$$

Here ϵ_λ is the energy flux conserved by the dynamical equations, ℓ is the scale of separation between two spatial points, and $\lambda = L/\ell$ is a scale ratio between some chosen fixed scale L and the scale ℓ. The velocity correlations of the underlying fluid parcel lead to similar correlations in the densities of a passively advected tracer (ρ) [*Obukhov*, 1949]:

$$\Delta\rho_\ell \equiv \langle |\rho(x+\ell)-\rho(x)| \rangle \simeq \langle \phi_\lambda^{1/3} \rangle \ell^{1/3}, \tag{2}$$

$$\phi = \chi^{1/2}\epsilon^{-1/6}, \tag{3}$$

where χ_λ is again a flux conserved by the dynamical equations.

It was observed [*Mandelbrot*, 1974; *Schertzer and Lovejoy*, 1987, 2011] that rather than being near-homogeneous, the fluxes $\epsilon_\lambda, \phi_\lambda$ behave as intermittent multifractal cascades that scale as

$$\langle \phi_\lambda^q \rangle \simeq \lambda^{K(q)}. \tag{4}$$

Here $K(q)$ captures the flux scaling profile and is called the "moment scaling function." In fact, the flux scaling can be expressed exactly as

$$\langle \phi_\lambda^q \rangle = (L_h/\ell)^{K(q)}, \tag{5}$$

where L_h has a meaning of the flux homogeneity scale. The flux homogeneity at the scale L_h can be seen from the following:

$$\langle \phi_{L_h}^q \rangle = \langle \phi_{L_h} \rangle^q. \tag{6}$$

Note that the equation (6) is obtained from the equation (5) by a trivial identity, since the fluxes have mean values equal to one. L_h is a physically interesting parameter, as it can be interpreted as the energy input scale. This is the initial scale of the cascade process, a scale from which the energy gradually dissipates, creating large inhomogeneities at the lowest scales.

The scaling continuity defined through the infinite divisibility and stability of the cascade in equation (4) implies that $K(q)$ is determined by a two-parametric family [*Schertzer and Lovejoy*, 1987, 2011] as

$$K(q) = \frac{C_1}{\alpha-1}(q^\alpha - q), \quad 0 \leq \alpha \leq 2, \alpha \neq 1. \tag{7}$$

Here C_1 and α are two free parameters, C_1 being a fractal codimension of the set giving dominant contribution to the mean and α is the Levy exponent describing how rapidly fractal dimensions of sets vary as they leave the mean singularity [*Gagnon et al.*, 2006]. For $\alpha = 1$ one gets the limiting expression:

$$K(q) = C_1 \cdot q\ln(q). \tag{8}$$

The case $\alpha = 2$ gives the lognormal model of turbulence [*Gurvitch and Yaglom*, 1967]. The model described by the equation (7) is called universal multifractals (UM).

A suitable generalization of passive scalar scaling is given by the fractionally integrated flux model (FIF) [*de Montera et al.*, 2011; *Schertzer and Lovejoy*, 1987, 2011]:

$$\Delta\rho_\ell^q \equiv \langle |\rho(x+\ell)-\rho(x)|^q \rangle = \tilde{K}^q \langle \phi_\ell^{aq} \rangle \ell^{Hq}. \tag{9}$$

In the equation (9) we have written explicitly the proportionality constant as $\tilde{K}$. The scaling model from the equation (9) is defined by four parameters: a, H, and the two UM parameters C_1, α. However, the universal multifractal (UM) scaling (equation (7)) can be used to reduce the number of parameters to three, by suitably redefining the C_1 and H values. The final model has then three parameters: the simple increments scaling exponent H and the two universal multifractal parameters C_1, α. One can intuitively understand the H, C_1, α parameters as follows: The scaling exponent H can be seen as a combined imprint of the dynamical drivers scaling (drivers such as solar energy, bathymetry, turbulence, etc.). If the imprint of those drivers was perfect, the fluctuations $\Delta\rho_\ell \simeq \ell^H$ would be constant across the domain. This is equivalent to the fluxes having codimension $C_1=0$, filling the whole physical space. However, in a realistic situation the mean value of the field fluctuations is realized only on a limited fraction of the underlying space. The size of this fraction then corresponds to the codimension $C_1 \neq 0$. The remaining fraction of the space with the fractal dimension C_1 corresponds to field fluctuations which deviate from their mean value. How much the field fluctuations deviate from their mean value is then partially controlled by the remaining α parameter.

The FIF model is sufficient to describe scale-invariance of fields in various areas of geophysics [*Gagnon et al.*, 2006; *Lavalee et al.*, 1993; *Lovejoy et al.*, 2001a,2001b; *Lovejoy and Schertzer*, 2010; *de Montera et al.*, 2011;

Seuront et al., 1996a,1996b; *Seuront and Lagadeuc*, 1997; *Seuront et al.*, 1999; *Seuront and Schmitt*, 2005a]. In *Skakala and Smyth* [2015] the FIF model was shown to describe the scaling of bathymetry, chlorophyll-a surface concentrations, and the sea surface temperature (SST) in the shelf seas around the south-west of the UK. The FIF model can be used for data parameterization as well as to determine the dominant dynamical drivers (using the multifractal parameters). For example, it is predicted that the 3D turbulent velocity fields have the following values of the FIF model parameters [*Schmitt et al.*, 1993]: $H=0.35\pm0.1$, $\alpha=1.3\pm0.1$, $C_1=0.25\pm0.05$. In general, for passive scalars the situation is less clear: in the 3D turbulent regime the H parameter seems to lie somewhere between $H=0.3-0.45$ and the α parameter between $\alpha=1.3-2$ [*Gagnon et al.*, 2006; *Lavalee et al.*, 1993; *Lovejoy et al.*, 2001b; *de Montera et al.*, 2011]. For SST the UM parameter values were found in *Lovejoy et al.* [2001b] as $\alpha=1.7\pm0.05$, $C_1=0.04\pm0.01$, and $H=0.42\pm0.02$. Deviations from the passive scalar regime can be identified with an action of specific drivers: for example in *Skakala and Smyth* [2015] the SST field distributions were interpreted as resulting from a combined effect of bathymetry scaling and turbulence.

2.2. Definition of Scaling-Based Model Skill Evaluation Metrics

There is not a single best way to compare two data sets and hence not a single best model skill evaluation metric. The use of a specific model skill evaluation metric rather depends on the questions asked and the purpose for which the specific model is used. Two types of data set comparisons (and metrics) are suggested in this section, both utilizing the scaling properties of the fluctuations from equation (9).

One could use inverse Mellin transform of the moments scaling function $K(q)$ to obtain the probability density distribution (PDF) for the field $\Delta\rho$ (equation (9)). The model and the EO data would lead to two different sets of C_1, α, H parameters, as well as to different L_h flux homogeneity scales (equation (5)) and proportionality constants (equation (9)). These would then give two different PDF's f_{EO}, f_{mod} that can be compared as

$$m=\int |f_{EO}(v)-f_{mod}(v)| \cdot dv. \tag{10}$$

Equation (10) suggests a natural metric, as it evaluates the differences in the structure of the two (EO and model) ensembles. However, there is one significant problem with the metric (10): the power tails of the two PDFs represent increasingly extreme events and eventually fail to correspond to the realistic, physically finite ensembles. The differences in the PDFs tails in the unphysical region can still, when integrated, provide a nontrivial contribution. This suggests that those PDFs tails should be removed from the integral (10). The solution is to multiply the integral (the equation (10)) by a weight that emphasizes the central peak of the distribution and discards the extreme tails. It turns out that the simplest way to do this is to work directly with the statistical moments. The analysis of the statistical moments provides us with the moment cutoff value q_D which corresponds to the largest singularity that can be sampled by the specific finite ensemble. Or in other words, q_D is the largest statistical moment which can be estimated from the finite ensemble [*Schertzer and Lovejoy*, 2011]. The cutoff moment q_D corresponds to a second-order phase transition [*Schertzer and Lovejoy*, 2011] and can be identified by a discontinuity in the second derivative of the moment scaling function $K(q)$. The discontinuity is a result of the fact that $K(q)$ behaves as a linear function for $q > q_D$ [*Schertzer and Lovejoy*, 2011].

In addition to this, the statistical moments provide us with a natural measure that emphasizes the values around the peak of the PDF:

$$UM_1=\int_0^{q_D} dq \left\langle \left| \frac{2 \cdot (\langle\Delta\rho_{(1)\ell}^q\rangle-\langle\Delta\rho_{(2)\ell}^q\rangle)}{\langle\Delta\rho_{(1)\ell}^q\rangle+\langle\Delta\rho_{(2)\ell}^q\rangle} \right| \right\rangle_\ell. \tag{11}$$

Here the $\rho_{(1)}, \rho_{(2)}$ represent two distributions whose fluctuations are being compared. The UM_1 metric measures the relative differences in statistical moments of the two distributions in the physical region $q \in (0, q_D)$. By relative differences one means differences weighted by the average between the statistical moments of the two distributions. This weight is largest for the moments that depend mostly on the peak of the PDF for $\Delta\rho$. Furthermore, to remove the scale dependence, the metric (11) averages across a range of scales at which the FIF model is a good approximation.

If we assume that the statistical moments of the two distributions do not differ too much then:

$$\langle \Delta \rho^q_{(1)\ell} \rangle - \langle \Delta \rho^q_{(2)\ell} \rangle = \sum_i \langle \Delta \rho^q_\ell \rangle_{,i} \Delta P_i, \tag{12}$$

where P_i are the model parameters. This simplifies the metric (11) into

$$UM_1 = \int_0^{q_D} dq \langle |\ln(\ell) \{A_\alpha \Delta\alpha + A_{C_1} \Delta C_1 + A_H \Delta H\} + A_{\tilde{K}} \Delta\tilde{K} + A_{L_h} \Delta L_h| \rangle_\ell. \tag{13}$$

The coefficients in the equation (13) can be expressed using the moment scaling function $K(q)$ (see the equation (6))

$$A_\alpha = -\frac{K(q)}{\alpha-1} + \frac{C_1}{\alpha-1} \ln(q) q^\alpha, \tag{14}$$

$$A_{C_1} = \frac{K(q)}{C_1}, \tag{15}$$

$$A_H = -q, \tag{16}$$

$$A_{\tilde{K}} = \frac{q}{\tilde{K}}, \tag{17}$$

$$A_{L_h} = \frac{K(q) - qH}{L_h}. \tag{18}$$

In case the integrand in the equation (13) has a constant signature one can further simplify the equation into:

$$UM_1 = |\langle \ln(\ell) \rangle_\ell \{A_\alpha \Delta\alpha + A_{C_1} \Delta C_1 + A_H \Delta H\} + A_{\tilde{K}} \Delta\tilde{K} + A_{L_h} \Delta L_h|, \tag{19}$$

with

$$A_\alpha = \frac{C_1 q_D^{\alpha+1}}{(\alpha-1)(\alpha+1)} \left[\ln(q_D) - \frac{2\alpha}{(\alpha-1)(\alpha+1)} \right] + \frac{C_1 q_D^2}{2(\alpha-1)^2}, \tag{20}$$

$$A_{C_1} = \frac{1}{\alpha-1} \left[\frac{q_D^{\alpha+1}}{\alpha+1} - \frac{q_D^2}{2} \right], \tag{21}$$

$$A_H = -\frac{q_D^2}{2}, \tag{22}$$

$$A_{\tilde{K}} = \frac{q_D^2}{2\tilde{K}}, \tag{23}$$

$$A_{L_h} = \frac{1}{L_h} \left[\frac{C_1 q_D^{\alpha+1}}{(\alpha-1)(\alpha+1)} - \left(H + \frac{C_1}{\alpha-1} \right) \frac{q_D^2}{2} \right]. \tag{24}$$

The coefficients A_i from the equations (20)–(24) can be used to estimate how sensitive is the metric UM_1 to the values of the various parameters. Imagine that UM_1 measures difference between two data sets that differ only in the value of one specific parameter. Consider a situation in which the data sets differ only in the parameter α and another situation when they differ only in the parameter H. Then the fluctuation in α changes the metric UM_1 by the same amount as the fluctuation in H if:

$$\frac{\Delta H}{\Delta \alpha} = \frac{A_\alpha}{A_H} = C_1 \left| \frac{2q_D^{\alpha-1}}{(\alpha-1)(\alpha+1)} \left[\ln(q_D) - \frac{2\alpha}{(\alpha-1)(\alpha+1)} \right] + \frac{1}{(\alpha-1)^2} \right|, \tag{25}$$

where A_α, A_H are from the equations (20) and (22). The same can be done with the C_1 and H coefficients

$$\frac{\Delta H}{\Delta C_1} = \frac{A_{C_1}}{A_H} = \frac{1}{\alpha-1} \left[\frac{q_D^{\alpha-1}}{\alpha+1} - 1 \right]. \tag{26}$$

As expected, the equations (25) and (26) show that the sensitivity of the metrics UM_1 on the values of the H, α, C_1 parameters depends significantly on the cutoff moment q_D. Smaller cutoff moment means more of
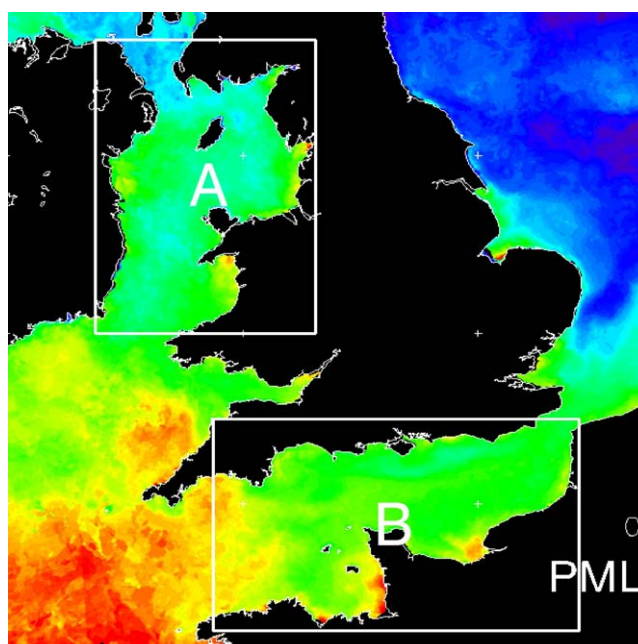
Figure 1. The AVHRR SST satellite weekly composite from 13–19 May 2011 with the two regions marked: (A) Irish Sea and (B) English Channel.

the PDF tail is discarded and the metric is relatively insensitive to the fluctuations of the C_1, α exponents, which determine the tail properties. Conversely, for large cutoff moments q_D the metric becomes more sensitive to the fluctuations of α, C_1, relative to the fluctuations of the mean value exponent H.

In addition to the metric UM_1 one might want to focus specifically on the three scaling exponents α, C_1, H, as they encode the dominant part of the information about the nature of the processes involved. To do this the second metric, UM_2, can be defined by simply taking UM_1 with $\Delta \tilde{K} = \Delta L_h = 0$.

The two metrics UM_1 and UM_2 defined in this section are both scale-free. The UM_1 metric carries complex information about fluctuations (including information about fluctuation sizes and the energy input scales), whereas the UM_2 metric is focused on the scaling exponents and carries more specific information about the dynamics at different scales. Since both UM_1 and UM_2 are based on relative differences between statistical moments, the closer the values of the two metrics are to zero, the better the match between the model and the EO data. Some additional intuition about how the values of UM_1 and UM_2 relate to the mean square root errors will be developed at the end of the Results section. Further to this, these metrics will be added to the standard metrics to evaluate the performance of the Finite-Volume, primitive equation Community Ocean Model (FVCOM) in the shelf seas around the south-west of the UK. This will be done in the next two sections of the paper.

2.3. Evaluation of the FVCOM Model
2.3.1. Data
All the data sets were taken from 2011 from which a complete FVCOM model run was available. The FVCOM model was configured and run by the co-authors at PML. The model configuration is described in *Cazenave et al.* [2016]. Two specific regions were considered: the Irish Sea region and the English Channel. The two regions are shown in Figure 1.

The model used in this study is the FVCOM, a prognostic, unstructured-grid, finite-volume, free-surface, 3D primitive equation coastal ocean circulation model [*Chen et al.*, 2003]. FVCOM solves the 3D momentum, continuity, temperature, salinity, and density equations by computing fluxes between unstructured triangular elements. Vertical turbulent mixing is modeled with the GOTM using a k-ϵ formulation [*Umlauf and Burhcard*, 2005] while horizontal mixing is parameterized through the Smagorinsky scheme [*Smagorinsky*, 1963]. The horizontal grid resolution in the model domain varies from 10 km at the open boundaries to 150 m in the finest coastal elements. The vertical grid in FVCOM is described in terrain following (sigma) coordinates with 20 quadratically distributed layers, where shallower areas resolve vertical structure with finer detail. The model is forced with TPXO [*Egbert et al.*, 1994; *Egbert and Erofeeva*, 2002] predicted tidal elevation at the open boundaries, with surface forcing (heat flux, wind and precipitation/evaporation) from the National Centers for Environmental Prediction and Department of Energy Atmospheric Model Intercomparison Project (NCEP-DOE AMIP-II) Reanalysis-2 data. River temperature climatology time series were calculated from the Environment Agency Freshwater River Temperature Archive [*Orr et al.*, 2010]. River discharges were obtained from the E-HYPE European catchment model [*Donnelly et al.*, 2012].
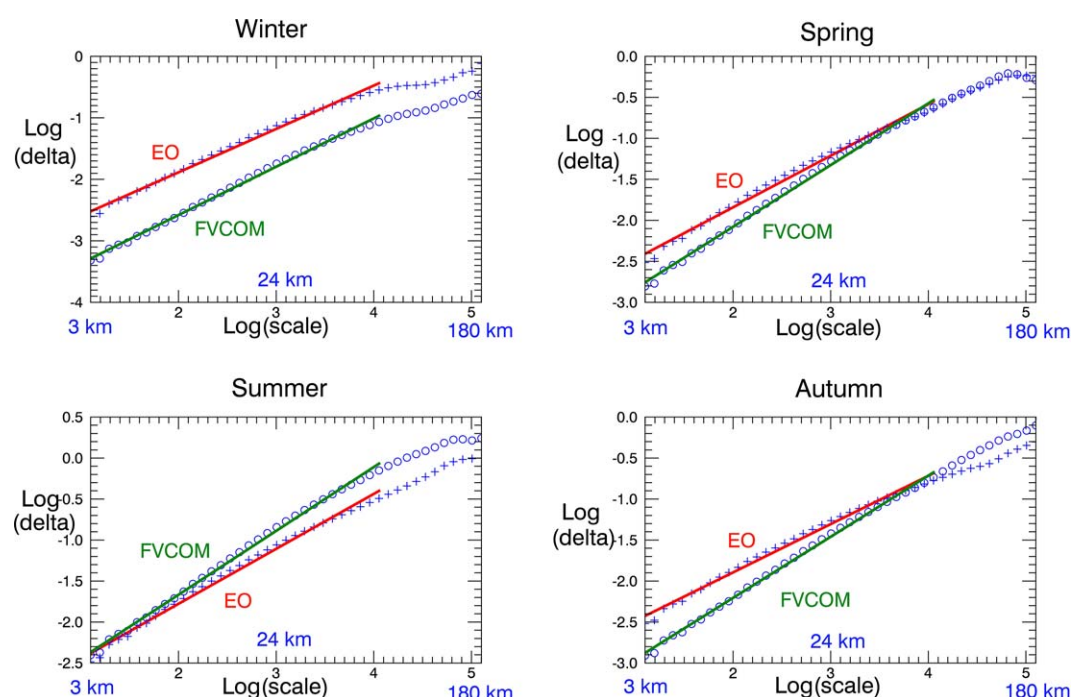
Figure 2. The Log-Log plot of the fluctuations $\Delta\rho$ ($q = 1$) as a function of scale. The figure shows seasonally averaged (Winter is January–March and so on) EO (red) and FVCOM (green) data in the Irish Sea. The slopes are the H coefficients from the Table 1.

FVCOM has been widely used in shelf and coastal domains for a range of problems where a strong need exists to resolve varying horizontal scales, including physical modeling of temperature and salinity stratification [*Chen et al.*, 2007; *Yang and Tarang*, 2008; *Huang*, 2011; *Zheng and Weisberg*, 2012]; modeling impacts from marine renewable energy devices [*Yang et al.*, 2013]; tracer evolution in complex estuaries [*Torres and Uncles*, 2011]; the behavior of sequestered CO_2 leak plumes [*Blackford et al.*, 2013]; and tracking the dispersal of lice [*Adams et al.*, 2012, 2014].

All the Earth Observation (EO) data were taken from the NOAA Advanced Very High Resolution Radiometer (AVHRR) satellite (the data resolution was 1.1 km). They were provided by the NERC Earth Observation Data Acquisition and Analysis Service (NEODAAS) at the Plymouth Marine Laboratory. For each month and region between 5 and 14 sufficiently cloud-free satellite overpasses were selected. Since satellite measures ocean skin with thickness of the order of 100 μm, whereas the model upper layer thickness can vary up to the order of ∼1 m, the ocean stratification introduces an error into the analysis. This is because one expects the horizontal ocean variability near the water surface to decrease with the vertical dimension. Furthermore, the solar radiation throughout the day overheats the ocean skin which is another potential source of error. To minimize these two sources of error only nighttime overpasses were considered.

2.3.2. Analysis

The FVCOM model data were collected from the same time than the EO overpasses. To remove some noise from the EO data, the data were averaged on the 3 pixel scale (∼3.3 *km*). The FVCOM model data were then put on a 3.3 *km* regular grid (through averaging). There was a number of pixels with missing data in both the EO and FVCOM data sets. The missing EO data are a result of the cloud cover, whereas in the FVCOM case the missing data are due to the grid sparsity further from the coastline (the FVCOM grid points are separated by distances of ≥ 10 *km* far from the coast). To retain consistency in the analysis, initially only data points valid in both data sets were considered. The missing data were then, in both cases, almost completely filled by an interpolation algorithm, where each empty sea pixel having at least one neighboring pixel containing data was filled with the average of the neighboring pixels data.

To determine the scaling properties, one starts with the scaling of the fluctuations $\Delta\rho_\ell$ (equation (9)). The scaling analysis was performed from the 7.5 km scale up to roughly the scale of 180 km (this upper bound
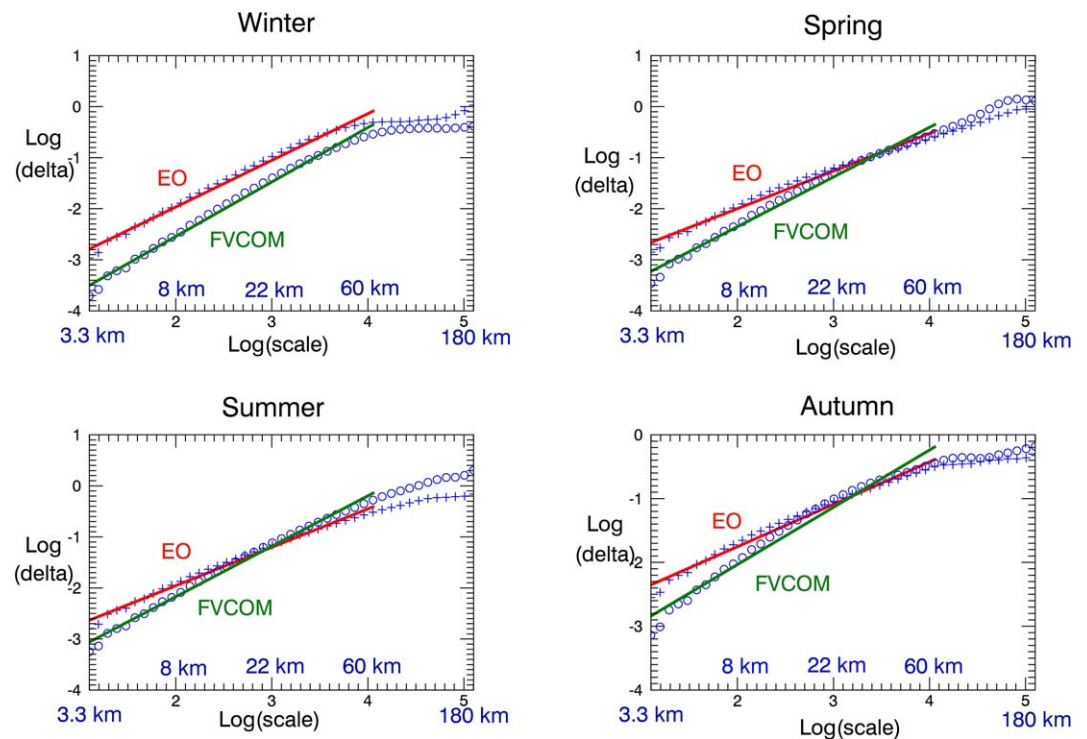
Figure 3. The Log-Log plot of the fluctuations $\Delta\rho$ ($q = 1$) as a function of scale. The figure shows seasonally averaged (Winter is January–March and so on) EO (red) and FVCOM (green) data in the English Channel. The slopes are the H coefficients from Table 1.
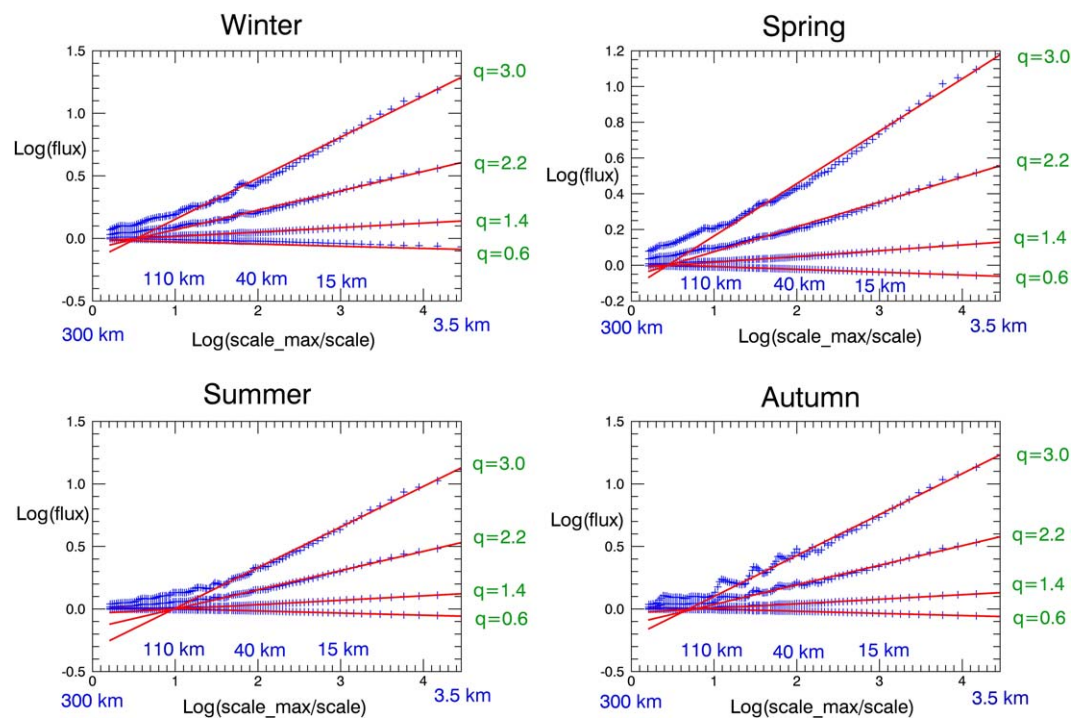

Figure 4. The seasonally averaged EO data fluxes Φ scaling in the Irish Sea. The Log-Log plot shows different statistical moments as a function of scale (blue points with red line fit).
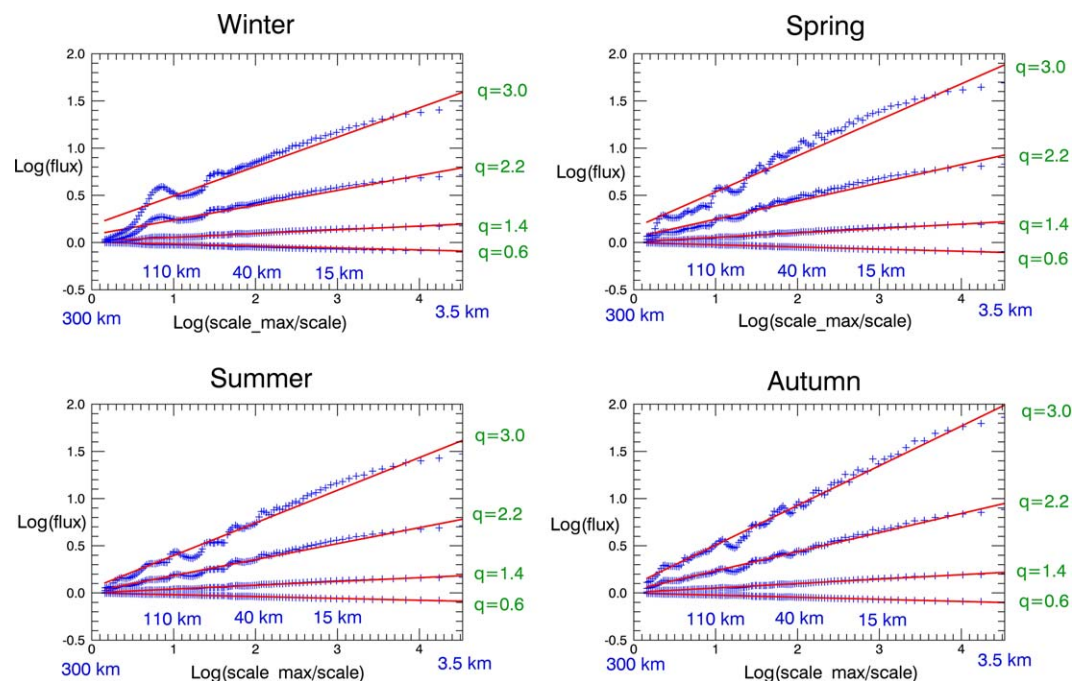
Figure 5. The seasonally averaged FVCOM model data fluxes Φ scaling in the Irish Sea. The Log-Log plot shows different statistical moments as a function of scale (blue points with red line fit).

was near the regional scales). The scale was increased in each step by 0.5%. The fluxes were estimated on the lowest scale by calculating $\Delta\rho_\ell/\langle\Delta\rho_\ell\rangle$. The flux scaling was determined from the $0 < q \leq 3$ moments of a cascade obtained by averaging the fluxes over bins with the area A (representing the scale $\ell=\sqrt{A}$). The moment scaling function $K(q)$ is determined from the slope of the linear regression of the Log-Log plot of each statistical moment as a function of scale. As mentioned in *Skakala and Smyth* [2015], one needs to resolve a conceptual problem with the regional boundaries and the missing pixels (mostly land). The problem was resolved here by the same algorithm as in *Skakala and Smyth* [2015]. The algorithm includes bins with lower number of pixels than $A=\ell^2$, but such bins are taken with a statistical weight proportional to the number of relevant pixels contained in the bin.
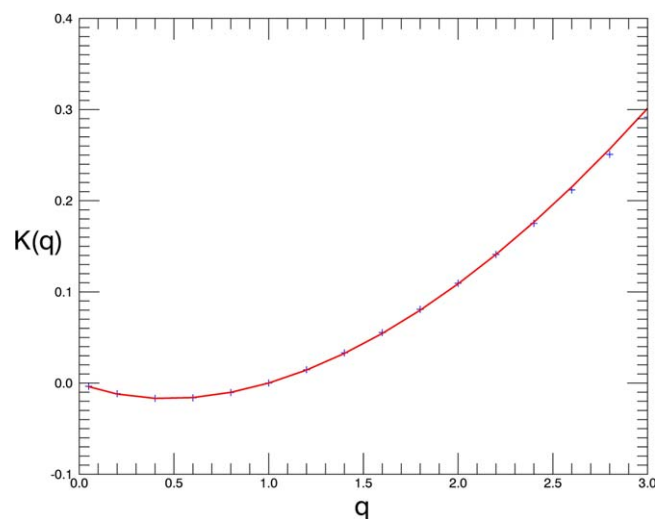
Finally, the scaling properties of the selected scenes were averaged throughout the monthly period for each single month of 2011. The FVCOM and EO data were then compared at the level of these monthly averages.

Figure 6. The plot shows an example of the moment scaling function $K(q)$ (for the EO data from English Channel from the October 2011). The points in the plot were calculated from the slopes of the different statistical moments and the full line shows the UM fit.

3. Results

We seasonally averaged the EO and FVCOM fluctuations $q = 1$ scaling and the results are shown in Figures 2 and 3. The seasonally averaged fluxes are shown for the Irish Sea in Figure 4 (EO data) and Figure 5 (FVCOM data). Figures 2–4 demonstrate that the SST fluctuations are well approximated for both EO and FVCOM data by the FIF

Table 1. The H, C_1, and α FIF Model Parameters Averaged Through the 2011 Year Overpasses[a]

Parameter	EO Irish	FVCOM Irish	EO English	FVCOM English
$\langle H \rangle$	0.557	0.651	0.655	0.839
$\langle C_1 \rangle$	0.091	0.136	0.114	0.204
$\langle \alpha \rangle$	1.721	1.598	1.67	1.485

[a]The table compares both EO and FVCOM parameter values in both regions (Irish Sea and English Channel).

model. Figures 2 and 3 show that the model fluctuations scale with a steeper profile than the EO fluctuations. Figure 2 further shows that the EO data fluctuations remain seasonally almost unchanged, whereas the model fluctuations depend strongly on the seasonality. The EO data fluctuations are in general larger, with the exception of the summer period in the Irish Sea. The fluxes scaling (Figures 4 and 5) show significant differences in the energy input scales L_h (see the equation (24)) for the EO data and for the FVCOM model data. The EO data outer scale lies in the range of $100-300 km$ (Figure 4), whereas the model outer scale is always larger than 500 km, with some values larger than 1000 km (Figure 5). The FVCOM model fluxes have steeper slopes than the EO fluxes, which indicates that the model dissipates energy at a higher rate than is observed in the EO data.

The universal multifractal (UM) fit (see the equation (7)) of the moment scaling function $K(q)$ had relative error <5% and in most of the cases the error was around 1%. The moment scaling function $K(q)$ for the English Channel and the October 2011 data is shown in Figure 6. The UM parameters were calculated for both EO and FVCOM data. The annual ensemble averages of the values of the H, C_1, and α parameters are shown in Table 1. The table shows a consistent difference between the FVCOM model and EO UM parameters: the model parameter C_1, H values are larger than the C_1, H values of the EO data (see Table 1), whereas the opposite is true for the α parameter. The correlation between the EO and the FVCOM multifractal parameters was relatively low, the Pearson coefficient was between 0.2 and 0.65, with larger values in the English Channel.

The models were compared with the EO data using three standard metrics: correlation coefficient, root-mean square error, and average error. In addition to that the two newly defined metrics UM_1 (equation (11)) and UM_2 were used. To use the UM_1 and UM_2 metrics the cutoff moments q_D were determined as $q_D \approx 5$. The five metrics are compared in Figure 7 (Irish Sea) and Figure 8 (English Channel). In the Irish Sea region (Figure 7) the three standard metrics (correlation coefficient, root-mean square error and average error) are mutually consistent and show a particularly poor match between the EO and the FVCOM data in the final months of the year. This is because the model has a tendency to overheat the upper ocean layer (the mean FVCOM SST was 1–2° larger than the EO SST). This tendency can be to some extent observed in the increase of UM_2 values, but is not shown by the UM_1 metric (see Figure 7). This is an interesting example showing that pixel-by-pixel based comparisons (R, root-mean square error, average error) and structural comparisons (UM_1, UM_2) can lead to very different results. In the English Channel (Figure 8), the picture is quite different, the values of all the
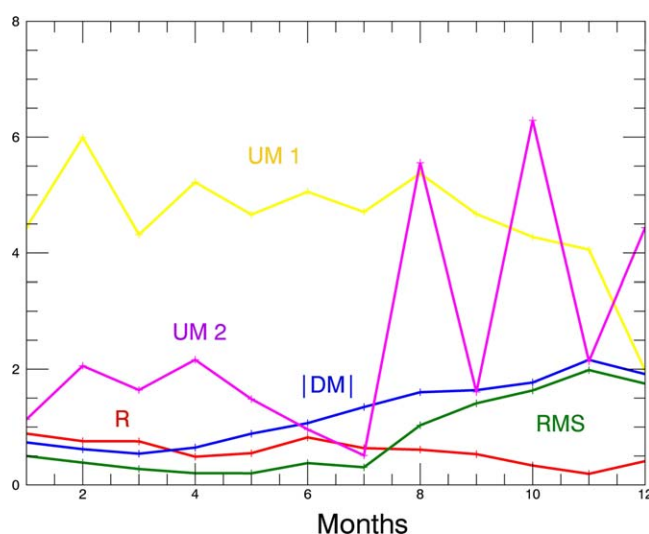

Figure 7. Comparison of different metrics for the Irish Sea region over 2011: (red) correlation coefficient, (blue) root mean square error, (green) absolute value taken from the average error, (yellow) the UM_1 metric comparing the overall size of fluctuations (the metric is defined by the equation (11)), (pink) the UM_2 metric comparing the scaling profiles. The values of the root mean square error and the average error are in $°C$, the remaining metrics are dimensionless.
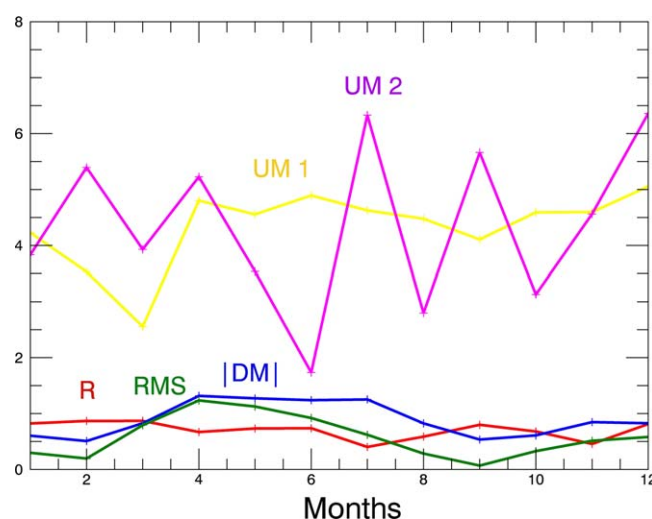
Figure 8. Comparison of different metrics for the English Channel region over 2011: (red) correlation coefficient, (blue) root mean square error, (green) absolute value taken from the average error, (yellow) the UM_1 metric comparing the overall size of fluctuations (the metric is defined by the equation (11)), (pink) the UM_2 metric comparing the scaling profiles. The values of the root mean square error and the average error are in degree Celsius, the remaining metrics are dimensionless.

metrics, change relatively little with time (except of fluctuations in UM_2), preserving the same seasonal profile.

To get a better insight into the typical range of values of UM_1 and UM_2, it is interesting to analyze how the scaling properties measured through UM_1, UM_2 evolve as one introduces noise into the data with some known properties. Gaussian noise with changing variance was redistributed across the data set, where the variance of the noise was correlated to the field value. Figure 9 compares the two data sets, the data set with the noise and the original data set without the noise, for different noise amplitudes. Figure 9 shows the values of the UM_1, UM_2 metrics as a function of the noise amplitude measured by the root mean square error. Let us say that the second data set matches well the first data set, if the

value of the root mean square error is bounded by $0.4°C$, which corresponds to the noise with variance about half of the natural variance of the data. Figure 9 then shows that the UM_1 and UM_2 values are bounded roughly by $UM_1 \approx 1$ and $UM_2 \approx 6$. As seen from the Figures 7 and 8, the FVCOM model fulfills this bound for the UM_2 metric, but not for the UM_1 metric. This suggests that the model captures well the overall field dynamics (data structural scaling properties), but poorly represents the outer scale of the energy input L_h (which was already discussed in the previous paragraph) and potentially also the overall size of the SST fluctuations.

4. Discussion

The selection of nighttime data minimized the effect of the upper layer stratification on the data scaling. Despite that, the steeper slopes observed in the model data scaling can be at least partly explained by the relative thick-

Figure 9. The figure shows the UM_1 (red) and UM_2 (green) values as a function of data-correlated Gaussian noise with the amplitude measured by the root-mean square error (RMS).

ness of the upper oceanic layer considered by the FVCOM model. Stratification decreases the horizontal variability on smaller scales and therefore tilts the scaling slope towards steeper angles. The seasonal change in stratification can also explain the matching slopes of the EO and FVCOM fluctuations in the winter season (Figures 2 and 3) and the seasonal variability in model fluctuations scaling (Figure 2). To explicitly confirm the hypothesis of the effect of stratification on the slope of the scaling, we split the English Channel region in Figure 1 into stratified (west) and mixed (east) regions [*Pingree and Griffiths*, 1978; *Simpson and Bowers*, 1981]. The scaling analysis in each of these two parts was then able to confirm the connection between stratification and the slope of the model data scaling.
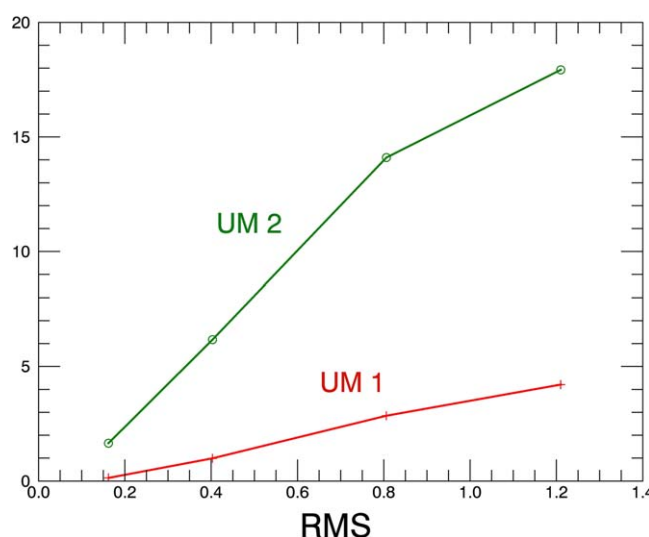
It was observed that the FVCOM model overheated the upper layer in the Irish Sea region. This explains why the metrics values in the Irish Sea region (see Figure 7) evolve relatively rapidly with time, especially when compared to the stationary situation in the English Channel region (Figure 8). The overheating is also responsible for the FVCOM fluctuations being larger than the EO fluctuations during summer and vice versa in winter (visible in the scaling analysis).

The scaling analysis is an important indicator of dominant dynamical drivers shaping the field distributions [*Skakala and Smyth*, 2015]. One expects turbulent eddies to be one of the main factors behind the SST scale correlations. Another important factor in the shelf seas is the overall shape of the basin described through the bathymetry scaling exponents. As previously observed [*Skakala and Smyth*, 2015], the bathymetry scaling profile can have a significant impact on the scaling profile of the fields. Furthermore, in the EO overpass imagery data, tidal currents (largely shaped by the bathymetry) can play a significant role in driving the field distributions. The bathymetry H scaling exponent is larger in the English Channel region ($H = 0.526$) than in the Irish Sea ($H = 0.302$), and this could explain larger values of the EO data H parameter in the English Channel, when compared to the Irish Sea region.

Unfortunately, the theoretical predictions for the large scale (>1 km) oceanic turbulence are ambiguous. There is no agreement in the literature if and how the effective two-dimensionality of the ocean at large scales (horizontal dimensions much larger than the vertical dimension) modifies the 3D turbulent model. This question is especially relevant in the shallow shelf seas (in our case mostly $<100m$). It has been suggested that the scaling exponents in the horizontal will remain the same as in case of 3D turbulence [*Lovejoy and Schertzer*, 2010], however, elsewhere [*Currie and Roff*, 2006], it is suggested that the two-dimensionality of the problem determines the value of the H exponent, which can lie anywhere between $H = 0.33$ and $H = 1$ ($H = 1$ being the ideal 2D turbulence value). Here it has been observed that the EO data scaling exponents H, C_1, and α (from Table 1) do not deviate too significantly from the SST scaling exponents observed on smaller scales in *Lovejoy et al.* [2001b]. Particularly, the α parameter values from Table 1 are within the predictions of *Lovejoy et al.* [2001b]: $\alpha = 1.7 \pm 0.05$. The model FIF parameters show larger deviations than the EO FIF parameters, but again, this can be explained by the stratification of the upper model layer.

5. Summary

The main purpose of this paper was to define two novel model skill evaluation metrics based on the universal scaling properties. Those metrics are scale-free and lead to an interesting structural comparison of the EO and the model data sets. Their particular advantage over the presently used metrics lies in their connection with the dominant dynamical drivers behind the field distributions. These metrics were applied to the FVCOM model in the shelf seas around the south-west of the UK: the paper attempts a comprehensive analysis of the model performance. Some quality bounds were estimated for the novel metrics and it was shown that the FVCOM model captures most of the dynamical features of the EO data, but it overestimates the outer scale of the energy input L_h, which leads to some discrepancies between the EO and the model data scaling. The two metrics already provide us with significant part of the information about how the model represents field dynamics. At present there is, however, still relatively large ambiguity in how the field dynamics maps into the multifractal scaling. To fully exploit the information carried by these metrics, the future research goal is to use models to obtain a more precise map between oceanographic drivers and the three-dimensional universal multifractal parameter space.

References

Allen, J. I., and P. J. Somerfeld (2009), A multivariate approach to model skill assessment, *J. Mar. Syst. 76*, 83–94.

Adams, T. P., K. Black, C. MacIntyre, and R. Dean (2012), Connectivity modelling and network analysis of sea lice infection in Loch Fyne, west coast of Scotland, *Aquaculture Environ. Interact.*, *3*, 51–63.

Adams, T. P., D. Aleynik, and M. T. Burrows (2014), Larval dispersal of intertidal organisms and the influence of coastline geography, *Ecography*, *37*, 698–710.

Allen, J. I., P. J. Somerfeld, and F. J. Gilbert (2007a), Quantifying uncertainty in high resolution coupled hydrodinamic-ecosystem models, *J. Mar. Syst. 64*, 3–14.

Allen, J. I., J. T. Holt, J. Blackford, and R. Proctor (2007b), Error quantification of a high-resolution coupled hydrodinamic-ecosystem coastal-ocean model: part 2. Chlorophyll-a, nutrients and SPM, *J. Mar. Syst. 68*(3–4), 381–404.

Allen, J. I., T. J. Smyth, J. R. Siddorn, and M. Holt (2008), How well can we forecast high biomass algal bloom events in a eutrophic coastal sea?, *Harmful Algae*, *8*, 70–76.

Bak, P., C. Tang, and K. Wiesenfeld (1987), Self-organized criticality: An explanation of $1/f$ noise, *Phys. Rev. Lett.*, *59*, 381–384.

Blackford, J. C., R. Torres, P. Cazaneve, and Y. Artioli (2013), Modelling dispersion of CO_2 plumes in sea water as an aid to monitoring and understanding ecological impact, *Energy Proc.*, *37*, 3379–3386.

Cazenave, P. W., R. Torres, and J. I. Allen (2016), Unstructured grid modelling of offshore wind farm impacts on seasonally stratified shelf seas, *Prog. Oceanogr.*, *145*, 25–41.

Chen, C., H. Liu, and R. C. Beardsley (2003), An unstructured grid, finite-volume, three-dimensional, primitive equations ocean model: Application to coastal ocean and estuaries, *J. Atmos. Ocean Tech.*, *20*, 159–186.

Chen C., H. Huang, R. C. Beardsley, H. Liu, Q. Xu, and G. Cowles (2007), A finite volume numerical approach for coastal ocean circulation studies: Comparisons with finite difference models, *J. Geophys. Res.*, *112*, C03018, doi:10.1029/2006JC003485.

Currie, W. J. S., and J. C. Roff (2006), Plankton are not passive tracers: Plankton in a turbulent environment, *J. Geophys. Res.*, *111*, C05S07, doi:10.1029/2005JC002967.

de Montera, L., M. Jouini, S. Verrier, S. Thiria, and M. Crepon (2011), Multifractal analysis of oceanic chlorophyll maps remotely sensed from space, *Ocean Sci.*, *7*, 219–229.

Doney, S. C., I. Limaa, J. K. Mooreb, K. Lindsayc, M. J. Behrenfeldd, T. K. Westberryd, N. Mahowalde, D. M. Glovera, and T. Takahashif (2008), Skill metrics for confronting global upper ocean ecosystem-biogeochemistry models against field and remote sensing data, *J. Mar. Syst.*, *76*, 95–112.

Donnelly, C., J. Rosberg, and K. Isberg (2012), A validation of river routing networks for catchment modelling from small to large scales, *Hydrol. Res.*, *44*, 917–925.

Egbert, G. D., and S. Y. Erofeeva (2002), Efficient inverse modeling of barotropic ocean tides, *J. Atmos. Oceanic Technol.*, *19*, 183–204.

Egbert, G. D., A. F. Bennett, and M. G. G. Foreman (1994), TOPEX/POSEIDON tides estimated using a global inverse model, *J. Geophys. Res.*, *99*, 24,821–24,852.

Gagnon, J. S., S. Lovejoy, and D. Schertzer (2006), Multifractal earth topography, *Nonlin. Processes Geophys.*, *13*, 541–570.

Gurvitch, A. S., and A. M. Yaglom (1967), Breakdown of eddies and probability distributions for small-scale turbulence, *Phys. Fluids*, *10*, 59–65.

Harte, D. (2001), *Multifractals: Theory and Applications*, Chapman and Hall, N. Y.

Huang, H. (2011), Finite volume coastal ocean model (FVCOM) 3D hydrodynamic model comparison, *Tech. Rep.*, La. State Univ., report number: 0904830891, The Portal to Texas History, UNT Libraries, Baton Rouge, La.

Jolliff, J. K., J. C. Kindleb, I. Shulmanb, B. Pentab, M. A. M. Friedrichsc, R. Helberb, and R. A. Arnoneb (2009), Summary diagrams for coupled hydrodynamic-ecosystem model skill assessment, *J. Mar. Syst. 76*, 64–82.

Kohonen, T. (2000), *Self-Organizing Maps*, 3rd ed., 528 pp., Springer, Berlin, Germany.

Kolmogorov, A. N. (1941), Local structure of turbulence in an incompressible liquid for very large Reynolds numbers, *Proc. Acad. Sci. URSS*, *30*, 299–303.

Lavalee, D., Lovejoy, S., Schertzer, D., and Ladoy, P. (1993), Nonlinear variability and landscape topography: Analysis and simulation, in *Fractals in Geography*, edited by L. deCola and N. Lam, pp. 171–205, Prentice Hall, N. J.

Lovejoy, S. (2014), A voyage through scales, a missing quadrillion and why the climate is not what you expect, *Clim. Dyn.*, *44*, 3187–3210.

Lovejoy, S., and D. Schertzer (2010), Towards a new synthesis for atmospheric dynamics: Space-time cascades, *Atmos. Res.*, *96*, 1–52.

Lovejoy, S., and D. Schertzer (2013), *The Weather and Climate: Emergent Laws and Multifractal Cascades*, Cambridge Univ. Press, Cambridge, U. K.

Lovejoy, S., D. Schertzer, and J. D. Stanway (2001a), Direct evidence of multifractal atmospheric cascades from planetary scales down to 1 km, *Phys. Rev. Lett.*, *86*(22), 5200.

Lovejoy, S., W. J. S. Currie, Y. Tessier, M. R. Claereboudt, E. Bourget, J. C. Roff, and D. Schertzer (2001b), Universal multifractals and ocean patchiness: phytoplankton, physical fields and coastal heterogeneity, *J. Plankton Res.*, *23*(2), 117–141.

Mandelbrot, B. (1974), Intermittent turbulence in self-similar cascades: Divergence of high moments and dimension of the carrier, *J. Fluid Mech.*, *62*, 331–358.

Mandelbrot, B. (1982), *The Fractal Geometry of Nature*, W. H. Freeman and Co., N. Y.

Mandelbrot, B. (1997), *Fractals and Scaling in Finance*, Springer, N. Y.

Novikov, E. A., and R. Stewart (1964), Intermittency of turbulence and spectrum of fluctuations in energy dissipation, *Izv. Akad. Nauk. SSSR, Ser. Geofiz.*, *3*, 408–412.

Obukhov, A. (1949), Structure of the temperature field in a turbulent flow, *Izv. Akad. Nauk. SSSR*, *13*, 55–69.

Orr, H. G., et al. (2010), Changing water temperatures: A surface water archive for England and Wales, in *Role of Hydrology in Managing Consequences of a Changing Global Environment*, edited by C. Kirby, Br. Hydrol. Soc, U. K.

Pingree, R. D., and D. K. Griffiths (1978), Tidal fronts on the shelf seas around the British Isles, *J. Geophys. Res.*, *83*, 4615–4622.

Radic, V., and G. Clarke (2011), Evaluation of IPCC models' performance in simulating late twentieth-century climatologies and weather patterns over North America, *J. Clim.*, *24*, 5257–5274.

Richardson, L. F. (1922), *Weather Prediction by Numerical Processes*, Cambridge Univ. Press, Cambridge, U. K.

Saux Picart, S., Butenschon, M., and J. D. Shutler (2012), Wavelett-based spatial comparison technique for analysing and evaluating two-dimensional geophysical model fields, *Geosci. Model Dev.*, *5*, 223–230.

Schertzer, D., and S. Lovejoy (1987), Physical modelling and analysis of rain and clouds by anisotropic scaling multiplicative processes, *J. Geophys. Res.*, *92*, 9693–9714, doi:10.1029/JD092iD08p09693.

Schertzer, D., and S. Lovejoy (1988), Multifractal simulations and analysis of clouds by multiplicative processes, *Atmos. Res.*, *21*, 337–361.

Schertzer, D., and S. Lovejoy (1997), Universal multifractals do exist!, *J. Appl. Meteorol.*, *36*, 1296–1303.

Schertzer, D., and S. Lovejoy (2011), Multifractals, generalized scale invariance and complexity in geophysics, *Int. J. Bifurcation Chaos*, *21*(12), 3417–3456.

Schmitt, F., D. Schertzer, S. Lovejoy, and Y. Brunet (1993), Estimation of universal for atmospheric turbulent multifractal indices velocity fields, *Fractals*, *01*, 568.

Seuront, L., and Y. Lagadeuc (1997), Characterization of space-time variability in stratified and mixed coastal waters (baie des Chaleurs, Québec, Canada): Application to fractal theory, *Mar. Ecol. Prog. Ser.*, *259*, 81–85.

Seuront, L., and F. G. Schmitt (2005a), Multiscaling statistical procedures for the exploration of biophysical couplings in intermittent turbulence; Part I. Theory, *Deep Sea Res., Part II*, *52*, 1308–1324.

Seuront, L., and F. G. Schmitt (2005b), Multiscaling statistical procedures for the exploration of biophysical couplings in intermittent turbulence; Part II. Applications, *Deep Sea Res., Part II*, *52*, 1325–1343.

Seuront, L., F. Schmitt, Y. Lagadeuc, D. Schertzer, S. Lovejoy, and S. Frontier (1996a), Multifractal analysis of phytoplankton biomass and temperature in the ocean, *Geophys. Res. Lett.*, *23*(24), 3591–3594.

Seuront, L. et al. (1996b), Multifractal intermittency of Eulerian and Lagrangian turbulence of ocean temperature and plankton fields, *Nonlinear Processes Geophys.*, *3*, 236–246.

Seuront, L., et al. (1999), Universal multifractal analysis as a tool to characterize multiscale intermittent patterns: Example of phytoplankton distribution in turbulent coastal waters, *J. Plankton Res.*, *21*, 877–922.

Seuront, L., H. Yamazaki, and F. Schmitt (2005), Intermittency, in *Marine Turbulence*, edited by H. Baumert, J. Simpson, and J. Sundermann, pp. 66–79, Cambridge Univ. Press, Cambridge, U. K.

Simpson, J. H., and D. Bowers (1981), Models of stratification and frontal movement in shelf seas, *Deep Sea Res., Part A*, *28*, 727–738.

Shutler, J. D., T. J. Smytha, S. Saux-Picarta, S. L. Wakelinb, P. Hyderc, P. Orekhova, M. G. Granta, G. H. Tilstonea, and J. I. Allen (2011), Evaluating the ability of a hydrodynamic ecosystem model to capture inter- and intra-annual spatial characteristics of chlorophyll-a in the north east Atlantic, *J. Mar. Syst.*, *88*, 169–182.

Skakala, J., and T. J. Smyth (2015), Complex coastal fields can be described by universal multifractals, *J. Geophys. Res.*, *120*, 6253–6265, doi: 10.1002/2015JC011111.

Smagorinsky, J. (1963), General circulation experiments with the primitive equations I: The basic experiment, *Mon. Weather Rev.*, *91*, 99–164.

Stow, C. A., J. Jolliffb, D. J. McGillicuddy Jr., S. C. Doneyc, J. I. Allend, M. A. M. Friedrichse, K. A. Rosef, and P. Wallheadg (2009), Skill assessment for coupled biological/physical models of marine systems, *J. Mar. Syst.*, *76*, 4–15.

Taylor, K. E. (2001), Summarizing multiple aspects of model performance in a single diagram, *J. Geophys. Res.*, *106*(7), 7183–7192.

Torres, R., and R. J. Uncles (2011), *Modeling of Estuarine and Coastal Waters*, vol. 2, Elsevier, Perth, Australia.

Umlauf, L., and H. Burhcard (2005), Second-order turbulence closure models for geophysical boundary layers. A review of recent work, *Cont. Shelf Res.*, *25*, 795–827.

Yaglom, A. M. (1966), The influence on the fluctuation in energy dissipation on the shape of turbulent characteristics in the inertial interval, *Sov. Phys. Dokl.*, *2*, 26–30.

Yang, Z., and K. Tarang (2008), Modeling of salt intrusion, intertidal mixing, and circulation in a braided estuary, *J. Coastal Res.*, *52*, 171–180.

Yang, Z., T. Wang, and A. E. Copping (2013), Modeling tidal stream energy extraction and its effects on transport processes in a tidal channel and bay system using a three-dimensional coastal ocean model, *Renewable Energy*, *50*, 605–613.

Zheng, L., and R. H. Weisberg (2012), Modeling the west Florida coastal ocean by downscaling from the deep ocean, across the continental shelf and into the estuaries, *Ocean Model.*, *48*, 10–29.